

Controlling the dynamical scale factor in a trapped atom Sagnac Interferometer

Yijia Zhou,¹ Igor Lesanovsky,^{1, 2} Thomas Fernholz,¹ and Weibin Li^{1, 2}

¹*School of Physics and Astronomy, University of Nottingham, Nottingham, NG7 2RD, UK*

²*Centre for the Theoretical Physics and Mathematics of Quantum Non-equilibrium Systems, The University of Nottingham, Nottingham, NG7 2RD, United Kingdom*

(Dated: May 26, 2022)

Sagnac interferometers with massive particles promise unique advantages in achieving high precision measurements of rotation rates over their optical counterparts. Recent proposals and experiments are exploring non-ballistic Sagnac interferometers where trapped atoms are transported along a closed path. This is achieved by using superpositions of internal quantum states and their control with state-dependent potentials. We address emergent questions regarding the dynamical behaviour of Bose-Einstein condensates in such an interferometer and its impact on rotation sensitivity. We investigate complex dependencies on atomic interactions as well as trap geometries, rotation rate, and speed of operation. We find that temporal transport profiles obtained from a simple optimization strategy for non-interacting particles remain surprisingly robust also in the presence of interactions over a large range of realistic parameters. High sensitivities can be achieved for short interrogation times far from the adiabatic regime. This highlights a route to building fast and robust guided ring Sagnac interferometers with fully trapped atoms.

Introduction. Atom interferometry [1] for precision measurements and quantum sensing [2] has become a powerful tool with applications ranging from fundamental physics [3] to absolute gravimetry [4] and inertial sensing [5, 6]. If the effect to be measured depends on length or inertial and gravitational forces, the scaling of sensitivity with particle mass in an atom interferometer, and thus signal gain by orders of magnitude, can be directly compared to its optical counterpart [7]. In a Sagnac interferometer, the resulting phase $\phi_S = 2\frac{m}{\hbar}A\omega_S$ can be used to measure rotation frequency ω_S . This phase is proportional to the (equivalent) mass m and the area A enclosed by the interferometer, factors which combine into the signal's scale factor $\partial\phi_S/\partial\omega_S$. Despite much smaller particle flux and enclosed interferometer area, atom interferometric gyroscopes rival commercial fibre-optic devices. Sensitivities below 10^{-9} rad/ \sqrt{s} [8], [9] with thermal beams and stability below 10^{-9} rad/s [10, 11] with free-falling, laser cooled ensembles have been demonstrated, see [12] for a recent review. In order to reduce apparatus size and to gain operational independence from specific conditions of gravitation and acceleration, a range of ring-shaped atom traps and guided interferometers have been proposed and implemented with various means, geometries, and objectives [13–25]. Large enclosed areas are desired, and multiple cycles [17] or, equivalently, resonator approaches [14] have been proposed, although the scaling of decoherence due to longer path lengths may limit the possible benefit over physically large areas [16].

The majority of approaches relies on ballistic motion of particles along a closed path, but the rotation-dependent Sagnac phase can equally be measured with fully trapped atoms, i.e. confined in three dimensions [20, 24]. In such a trapped Sagnac interferometer (TSI) atomic motion is actively controlled. The necessary beam splitting and recombination arise from coherent internal state operations

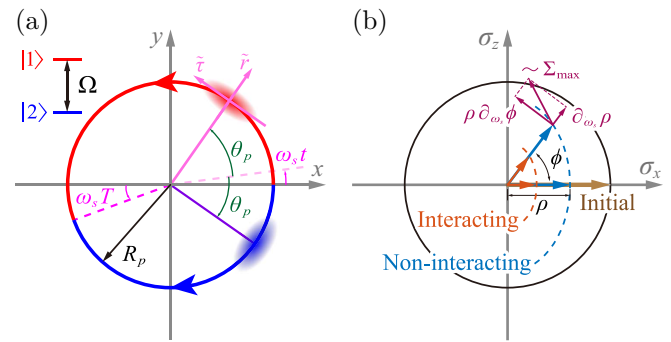


FIG. 1. External and internal dynamics of the Sagnac interferometer. (a) Atoms in a coherent superposition of two internal states $\{|1\rangle, |2\rangle\}$ (coupled with Rabi frequency Ω) are initially located on the x -axis and transported along opposite paths. In the depicted inertial frame, the external, anti-clockwise rotation at ω_s forces the $|1\rangle$ -component (red, top path) to travel a longer distance than the $|2\rangle$ -component (blue, bottom path). This induces a Sagnac phase between the two states. (b) Bloch vector representation of collective, internal states and interferometer sensitivity. State vectors are shown in the $\sigma_x - \sigma_z$ plane. Referenced to the initial state (brown arrow), the final states (blue and red arrows) acquire a phase ϕ and show reduced contrast ρ . Those two quantities depend on the external rotation ω_s (dashed curves), dynamical factors, and interactions. The total change of the Bloch vector with respect to ω_s determines the interferometer sensitivity.

in conjunction with state-dependent potentials. Fully trapped atoms promise some important advantages. Interference can be observed without a standing wave phase pattern, which may require high imaging resolution [23] and interferometric stability with respect to a reference that is external to the trap, e.g. camera position or a standing wave light field. Particles can be accelerated to high speeds on path enclosing large areas within short

times, a goal pursued by experiments on large momentum beam splitters [26–28]. Atomic wave packets do not disperse and their transport can be well controlled against gravity and external acceleration, where, in contrast, ballistic operation will affect the cycle time and may even preclude the enclosure of a large physical area.

Both guided and trapped interferometers have not yet reached maturity, and some intrinsic effects received only little attention so far. These include excitation of higher trap modes by internal and external forces, such as centripetal forces [21], potential corrugations, external acceleration, and vibration. These will affect timing, enclosed area, and interferometer contrast, and understanding their impact is complicated further by atomic interactions, quantum degeneracy and dimensionality of the atomic ensemble. These effects alter the proportionality between the measured signal and rotation, i.e. the *scale factor*, which is not simply given by the static factors that enter the expression for the Sagnac phase. An actual measurement is rather determined by a more involved, dynamical dependence of the interferometer output on external rotation, which defines a dynamical scale factor.

In this work, we investigate the dynamical scale factor for the case of a trapped two-mode Bose-Einstein condensate (BEC) and analyse a simple optimization scheme to achieve robust sensitivities, focussing on the slow rotation regime. Maximal sensitivities can be obtained when the spatial wave functions in the two interferometer arms remain identical. However, the transport will excite opposing centre-of-mass motions in the trap, and these are not necessarily anti-symmetric between the two arms due to external rotation and atomic interactions. The path-dependent excitation severely reduces interferometer sensitivities. Through optimizing time-dependent driving profiles of the transport potential, we can robustly achieve near-maximal sensitivities at short interrogation times regardless of atomic interactions.

Interferometer Model. We consider an ensemble of atoms with two internal states $\{|1\rangle, |2\rangle\}$, as depicted in Fig. 1a. These can be hyperfine levels of alkali atoms (e.g. Rb, Cs). Atoms can be put into coherent superposition of internal (clock) states and transported in opposite directions along a ring by state-dependent traps [13, 24, 29], which are guided along a ring with radius R_p , as shown in Fig. 1a. For simplicity, we assume strong confinement in the direction perpendicular to the ring (z -axis) assuming that the system remains in the ground state in this direction. The dynamics of the BEC are governed by two coupled, two-dimensional (2D) Gross-Pitaevskii equations (GPEs) [30],

$$i\hbar \frac{\partial}{\partial t} \psi_j = \left(h_j + g_{jk} |\psi_k|^2 \right) \psi_j + \frac{\Omega}{2} \psi_k, \quad (1)$$

where $j, k = 1, 2$ and $j \neq k$ are labelling the two internal states (components). The order parameter ψ_j is normalized, $\int |\psi_j|^2 dr = 1$. The j -th component Hamiltonian is

given by

$$h_j = -\frac{\hbar^2}{2m} \nabla_j^2 + \frac{m\omega_r^2}{2} \tilde{r}_j^2 + \frac{m\omega_\tau^2}{2} \tilde{\tau}_j^2 + g_{jj} |\psi_j|^2,$$

where m is the atomic mass and ω_r (ω_τ) are the trapping frequencies in the radial (azimuthal) directions. In Eq. (1), we have defined local coordinate vectors $\tilde{r}_j = (x - R_p \cos \Theta_j) \cos \Theta_j - (y - R_p \sin \Theta_j) \sin \Theta_j$ and $\tilde{\tau}_j = (x - R_p \cos \Theta_j) \sin \Theta_j + (y - R_p \sin \Theta_j) \cos \Theta_j$, with respect to the trap centres at $\Theta_j(t) = \pm\theta_p(t) + \omega_s t$. The trap centers are determined by the *driving function* $\theta_p(t)$ and the external rotation of angular frequency ω_s that is to be measured. The boundary conditions for the driving function are $\theta_p(0) = 0$ and $\theta_p(T) = \pi$. The coefficients $g_{jk} = 2\sqrt{2\pi N \hbar^2 a_{jk}} / (ml_z)$ quantify the strengths of intra-state ($j = k$) and inter-state ($j \neq k$) interactions, which depend on the number of particles N , and the effective s -wave scattering lengths a_{jk} under the out-of-plane confinement to length l_z [31]. For convenience, we scale time, energy and length according to $t_s = 1/\omega_r$, $E_s = \hbar\omega_r$ and $l_s = \sqrt{\hbar/2m\omega_r}$ in the following unless stated elsewhere.

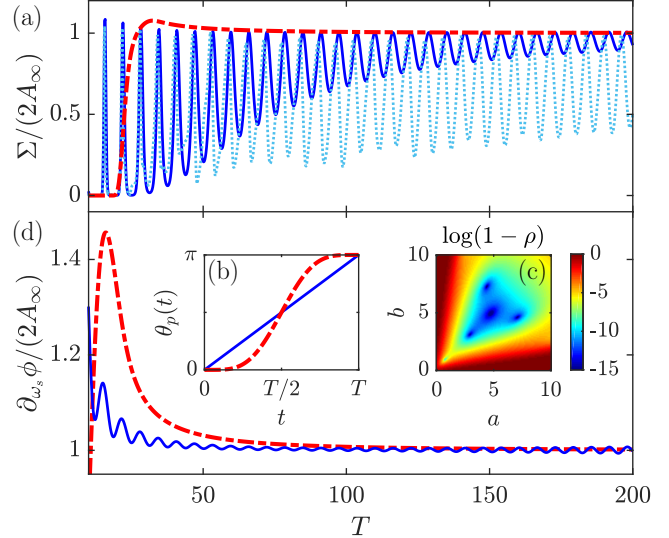


FIG. 2. **Sensitivity and optimized driving function.** (a) Sensitivity as a function of T for linear driving without (solid) and with interaction $g_{11} = g_{22} = g_{12} = 30$ (dotted). When applying an optimized driving function with parameters $a = b = 4$ [see text for and panel (b) details], the oscillations are suppressed and the sensitivity approaches the static value for $T > 30$ (dashed). (b) Driving function for constant speed ($a = b = 0$, solid), and optimal driving with $a = b = 4$ (dashed). (c) Interferometer contrast ρ as a function of the parameters a and b of the profile (5) for an interrogation time of $T = 50$. (d) Behavior of the rotation dependent phase factor of the interferometer without (solid) and with (dashed) optimization.

Sensitivity of the Sagnac interferometer. To operate the TSI, we first create a coherent superposition state

$(|1\rangle + |2\rangle)/\sqrt{2}$ by performing a fast $\pi/2$ -pulse on a BEC in the internal state $|1\rangle$. The two states are then guided along a ring in opposite directions (see Fig. 1a). When they are recombined after the interrogation time T [12], a second fast $\pi/2$ -pulse is applied to convert the accumulated phase difference into a population difference between the two states. The rotation frequency ω_s is then encoded in the expectation value $\langle\sigma_z\rangle = N_2 - N_1$.

The figure of merit is the interferometer sensitivity, which measures changes of $\langle\sigma_z\rangle$ with respect to rotation ω_s ,

$$\Sigma(\omega_s) = \frac{\partial\langle\sigma_z\rangle}{\partial\omega_s} = \frac{\langle\sigma_z\rangle}{\rho} \frac{\partial\rho}{\partial\omega_s} + \rho \cos\phi \frac{\partial\phi}{\partial\omega_s}. \quad (2)$$

Here, we used the parameterization $\langle\sigma_z\rangle = \rho \sin\phi$, where ρ and ϕ describe length (contrast) and orientation (phase) of the Bloch vector, see Fig. 1b. Both quantities are determined by the spatial overlap of the two states $\int \psi_2^*(\mathbf{r}, T) \psi_1(\mathbf{r}, T) d\mathbf{r} = \rho e^{i\phi}$ [20] (see Supplementary for details).

The scale factor Eq. (2) has two contributions. However, in the slow rotation limit $\omega_s \rightarrow 0$, the derivative $\partial\rho/\partial\omega_s$ vanishes because ρ must be an even function of ω_s . Here, the maximum sensitivity (obtained by setting the phase reference such that $\phi = 0$ at $\omega_s = 0$) reduces to

$$\tilde{\Sigma} = \Sigma(\omega_s = 0) = \rho \frac{\partial\phi}{\partial\omega_s} \Big|_{\omega_s=0}, \quad (3)$$

which solely depends on ρ and the phase gradient $\partial\phi/\partial\omega_s$. In the following we will investigate how these two parameters depend on the atomic interaction, the trap aspect ratio, and the interrogation time T .

First, we consider a simple linear driving profile $\theta_p(t) = t\pi/T$ and the case of a non-interacting BEC. Fig. 2a shows the sensitivity obtained by numerically solving the coupled GPEs with a small rotation (we take $\omega_s = 10^{-3}\omega_r$ and $R_p = 10$, throughout the work). The sensitivity oscillates as a function of the interrogation time T , with decreasing amplitude for increasing T [20]. In the limit $T \rightarrow \infty$, the sensitivity is approximately given by

$$\tilde{\Sigma}_\infty \approx \frac{2A_\infty}{[1 - (\pi/T)^2]^2}. \quad (4)$$

It thus approaches the conventional scale factor $2A_\infty$, where $A_\infty = \pi R_p^2$ is the area of the ring (in scaled units of l_s^2). This dependence provides a first example for a *dynamical* scale factor: the centrifugal forces lead to an increase in the area enclosed by the atomic trajectories. This effect is present in higher dimensions (2D and 3D) whilst absent in 1D models.

Sensitivities change qualitatively when inter- and intra-state interactions are taken into account. We observe that the oscillations of sensitivity increase drastically at intermediate interrogation times, and their amplitudes decrease much slower with increasing T (Fig. 2a)

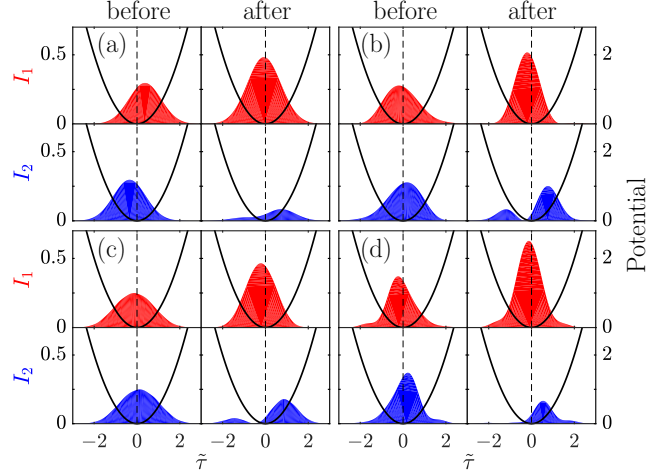


FIG. 3. **Internal BEC dynamics.** Spatial densities of the BEC components projected on the $\tilde{\tau}$ direction. Density snapshots of the states $|1\rangle$ (upper row) and $|2\rangle$ (lower row) immediately before and after the second (recombination) $\pi/2$ -pulse are shown in each panel. Panels correspond to different interaction strengths: (a) $g_{11} = g_{22} = g_{12} = 0$, (b) $g_{11} = g_{22} = g_{12} = 30$, (c) $g_{11} = g_{22} = 30, g_{12} = 0$, and (d) $g_{11} = g_{22} = 0, g_{12} = 30$. The parameters used in the calculations are $\omega_r = \omega_\tau = 1$, $T = 100$. The trapping potential (solid) and trap centre (dashed) along the $\tilde{\tau}$ axis (see main text for details) are shown.

than for the non-interacting case. The reduction of sensitivity arises from the fact that collective modes of the BEC are excited when atoms are transported non-adiabatically [32] around the ring. To illustrate this, we evaluate the projected BEC densities on the $\tilde{\tau}$ axis, $I_j = \int d\tilde{\tau} |\psi_j|^2$ right before and right after the second $\pi/2$ -pulse. As shown in Fig. 3a for a non-interacting BEC, the densities of the individual components may be shifted oppositely from the trap center before the second pulse, leading to incomplete conversion of (zero) phase into population difference. In addition, the density profiles change with increasing interaction strengths (Fig. 3b-d). When intrastate interactions dominate (Fig. 3d), the wave packets distort significantly from a Gaussian shape during the transport.

Optimization for a non-interacting BEC. In the following we aim to avoid the path dependent excitation of the BEC components in order to reach maximal sensitivity $\tilde{\Sigma}_\infty$ also for short interrogation times. Previous studies [20, 33] have considered ideal driving functions of a non-interacting BEC by excluding frequency components at the trapping frequency, $\int_0^T \sin[\theta_p(\tau)] e^{i\tau} d\tau = 0$. However, this condition does not avoid oscillations during the transport and it is insufficient when interactions are non-negligible.

During the transport, the BEC should be accelerated (decelerated) slowly at $t \rightarrow 0$ ($t \rightarrow T$) to avoid dynamical excitations, which is satisfied by the nonlinear driving

function

$$\theta_p(t) = \frac{\pi}{B(a+1, b+1)} \int_0^t \left(\frac{t'}{T}\right)^a \left(1 - \frac{t'}{T}\right)^b dt', \quad (5)$$

where the (Beta-)function $B(a, b)$ ensures normalization, to meet the boundary condition $\theta_p(T) = \pi$. This driving function is a convenient choice and has been applied to other optimization problems, e.g., conformal antenna arrays [34]. It generally has a sigmoidal form as shown and includes the linear ramp as a limiting case, as shown in Fig. 2c.

Using this driving function, the sensitivity for a non-interacting BEC is shown in Fig. 2a as a function of the interrogation time T . The oscillations have vanished and the sensitivity quickly approaches the value $\tilde{\Sigma}_\infty$ already at short times. Note, that this behavior is largely independent of precise choice of the parameters a and b , which can be seen in Fig. 2d.

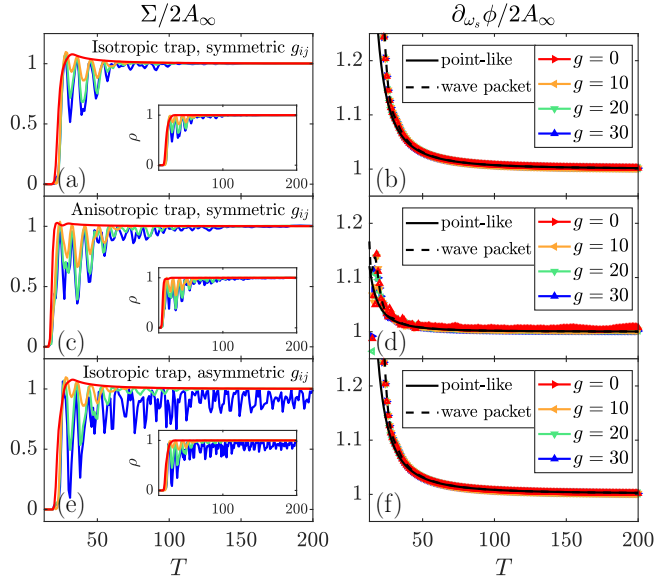


FIG. 4. Role of trap anisotropy and interactions. Sensitivity, normalized to static scale factor, (left column) and phase gradient (right column) as a function of interrogation time T for the driving function parameters $a = b = 4$. We consider three cases: (a,b) symmetric interactions $g_{11} = g_{22} = g_{12} = g$ and isotropic traps $\omega_r = \omega_\tau = 1$, (c,d) symmetric interactions $g_{11} = g_{22} = g_{12} = g$ and anisotropic traps $\omega_r = 1$, $\omega_\tau = 0.5$, (e,f) asymmetric interactions $g_{11} = g_{22} = 10$, $g_{12} = g$ and anisotropic traps $\omega_r = \omega_\tau = 1$. Insets in the left panels show the contrast ρ . The phase gradients are displayed together with numerical calculations of the path-enclosed area for a classical point-like particle (black solid lines) and an average over the BEC wave packets (dashed lines).

Application to an interacting BEC. To study a TSI implemented with an interacting BEC, we first consider a scenario where atomic interactions are symmetric ($g_{11} = g_{22} = g_{12} = g$) and the trapping potentials are isotropic ($\omega_r = \omega_\tau$). We use the same driving function

$\theta_p(t)$ as in the case of a non-interacting BEC. In Fig. 4a, the resulting sensitivities are presented for various interaction strengths g . Although oscillations of the sensitivity reemerge with stronger interactions, their amplitudes quickly decrease with increasing T . For the strongest interactions considered in these examples ($g = 30$), the sensitivity settles near the maximal value $\tilde{\Sigma}_\infty$ for $T > 100$.

Similar observations hold in the case of anisotropic trapping potentials (Fig. 4c,d) as well as for non-symmetric atomic interactions (Fig. 4e,f). The sensitivities slightly decrease as the traps become anisotropic and also when the inter- and intra-state interactions differ, i.e. $g_{11} = g_{22} = g \neq g_{12}$. We find that robust sensitivities can be obtained when g_{12} is smaller or comparable to g . However, the optimized (non-interacting) driving function becomes less efficient when g_{12} is much greater than g . We attribute this to the fact that strong repulsion [32] between the two BEC components causes immiscibility and prevents them from overlapping in space (see Fig. 3d), leading to reduced contrast. This, however, is not a major issue in realistic experiments as the inter- and intra-state scattering lengths can be very similar (e.g. Rb atoms).

An interesting observation is that in all the considered cases, the sensitivity is mostly influenced by a reduction of contrast rather than through the phase gradient. This can be seen by the very similar dependencies of sensitivity and contrast on the interrogation time T , as shown in the insets to Fig. 2a,b,c. The sensitivity exhibits a weak dependence on the phase gradient at intermediate interrogation times $20 < T < 50$ (see Fig. 4b,d,f), where values going beyond the static scale factor are achieved due to non-negligible centrifugal forces. An important finding is that the phase gradient is largely immune to atomic interactions and trap geometry, which we attribute to the suppression of radial center-of-mass oscillations also in the presence of interactions. As shown in Fig. 4b,d,f, and similar to the optimized response in Fig. 2d, the phase gradient decreases smoothly with increasing T , approaching the static scale factor for $T \rightarrow \infty$. In fact, the scale factor agrees closely with numerical calculations of the path enclosed area for a point-like classical particle (see Supplementary for details) as well as a refined calculation where we weigh the point-particle's position with the BEC wave packet. Therefore, an accurate measurement of rotation can be obtained by adaptive phase estimation protocols that co-estimate the contrast also in the case of uncertain dynamics [35, 36].

Conclusion. We analyzed the dependence of the dynamical scale-factor of guided Sagnac interferometers in the slow rotation regime with respect to transport parameters, atomic interactions, and trap symmetry. Employing a simple optimized driving function for the transport of atoms in state-dependent potentials reduces path-dependent excitations and achieves maximal sensitivities at moderate interrogation times, typically tens of trap

oscillation periods, for both ideal and interacting BECs. Our theoretical study is important to guide current experimental efforts on building robust and fast Sagnac interferometers with fully trapped atomic gases. It lays a foundation for further analyses of other experimentally relevant parameters, such as atom number fluctuations [37, 38], imperfect state operations, and finite temperatures [20].

We thank M. Fromhold, M. Greenaway, G. Raggi, S. Wu for fruitful discussion. We are grateful for access to

the University of Nottingham High Performance Computing Facility. Y. Zhou is supported by China Scholarship Council (CSC) No. 201606100035. The research leading to these results has received funding from the European Research Council under the European Unions Seventh Framework Programme (FP/2007-2013)/ERC Grant Agreement No. 335266 (ESCQUMA) as well as from the Engineering and Physical Sciences Research Council (Grant Nr. EP/M013294/1). I.L. gratefully acknowledges funding through the Royal Society Wolfson Research Merit Award.

SUPPLEMENTAL MATERIAL FOR "CONTROLLING THE DYNAMICAL SCALE FACTOR IN A TRAPPED ATOM SAGNAC INTERFEROMETER"

DERIVATION OF THE SENSITIVITY

The state of the two-component BEC is represented by a spinor,

$$\Psi(t) = \frac{1}{\sqrt{2}} \begin{pmatrix} \psi_1(\mathbf{r}, t) \\ \psi_2(\mathbf{r}, t) \end{pmatrix}, \quad (6)$$

where $\psi_1(\mathbf{r}, t)$ and $\psi_2(\mathbf{r}, t)$ denote the spatial wave functions corresponding to the internal states $|1\rangle$ and $|2\rangle$, respectively. Applying the coupling field with Rabi frequency Ω is equivalent with multiplying the spinor with the operator,

$$\hat{R}_\varphi(\theta_r, \phi_r) = \begin{pmatrix} \cos \frac{\varphi}{2} - i \sin \frac{\varphi}{2} \cos \theta_r & -i \sin \frac{\varphi}{2} \sin \theta_r e^{-i\phi_r} \\ -i \sin \frac{\varphi}{2} \sin \theta_r e^{i\phi_r} & \cos \frac{\varphi}{2} + i \sin \frac{\varphi}{2} \cos \theta_r \end{pmatrix}. \quad (7)$$

where $\varphi = \Omega t/2$ is the pulse area and (θ_r, ϕ_r) are reference phases.

The first $\pi/2$ -pulse of the interferometer protocol creates a superposition state of $|1\rangle$ and $|2\rangle$ with equal populations, $\int |\psi_1(\mathbf{r}, t=0)|^2 d\mathbf{r} = \int |\psi_2(\mathbf{r}, t=0)|^2 d\mathbf{r}$. After the interrogation time T the atoms are subject to a second $\pi/2$ -pulse, after which the average population difference is given by

$$\begin{aligned} \langle \hat{\sigma}_z \rangle &= \left\langle \Psi(T) \left| \hat{R}_{\pi/2}^\dagger(\theta_r, \phi_r) \hat{\sigma}_z \hat{R}_{\pi/2}(\theta_r, \phi_r) \right| \Psi(T) \right\rangle \\ &= \frac{1}{2} \cos^2 \theta_r \int (|\psi_1(\mathbf{r}, T)|^2 - |\psi_2(\mathbf{r}, T)|^2) d\mathbf{r} + \text{Re} \left[\sin \theta_r e^{i\phi_r} (\cos \theta_r + i) \int \psi_1^*(\mathbf{r}, T) \psi_2(\mathbf{r}, T) d\mathbf{r} \right] \\ &= \rho \sin \theta_r [\cos \theta_r \cos(\phi - \phi_r) + \sin(\phi - \phi_r)]. \end{aligned} \quad (8)$$

Here we have introduced the spatial overlap $\int \psi_1(\mathbf{r}, T) \psi_2^*(\mathbf{r}, T) d\mathbf{r} = \rho e^{i\phi}$.

Using the fact that $\partial \rho / \partial \omega_s = 0$ at $\omega_s = 0$ (see main text), we find the sensitivity to be

$$\frac{\partial \langle \hat{\sigma}_z \rangle}{\partial \omega_s} = \sin \theta_r [-\cos \theta_r \sin(\phi - \phi_r) + \cos(\phi - \phi_r)] \rho \frac{\partial \phi}{\partial \omega_s}, \quad (9)$$

whose maximum is achieved when setting the reference phases $\theta_r = \pi/2$ and $\phi_r - \phi = k\pi$ with k being an integer.

ANALYTICAL SOLUTIONS FOR TWO DIMENSIONAL BECS

The dynamics of two-dimensional non-interacting BECs can be solved analytically. To this end we first transform to a rotating frame with angular frequency ω_s using unitary operator $\hat{U}_{1,2}(t) = \exp [i\omega_s t \hat{L}_z] = \exp [\omega_s t (x \frac{\partial}{\partial y} - y \frac{\partial}{\partial x})]$.

The Hamiltonians h_1 and h_2 (with $g_{11} = g_{22} = 0$), which are given in the main text, then become

$$\begin{aligned}\hat{h}'_{1,2} &= \hat{U}_{1,2}\hat{h}_{1,2}\hat{U}_{1,2}^\dagger + i\hat{U}_{1,2}^\dagger \frac{\partial}{\partial t}\hat{U}_{1,2} \\ &= -\frac{1}{2} \left(\frac{\partial^2}{\partial x^2} + \frac{\partial^2}{\partial y^2} \right) + \frac{1}{2} (x^2 + y^2 + R_p^2) - R_p x \cos \theta_p(t) \mp R_p y \sin \theta_p(t) + i\omega_s \left(x \frac{\partial}{\partial y} - y \frac{\partial}{\partial x} \right).\end{aligned}\quad (10)$$

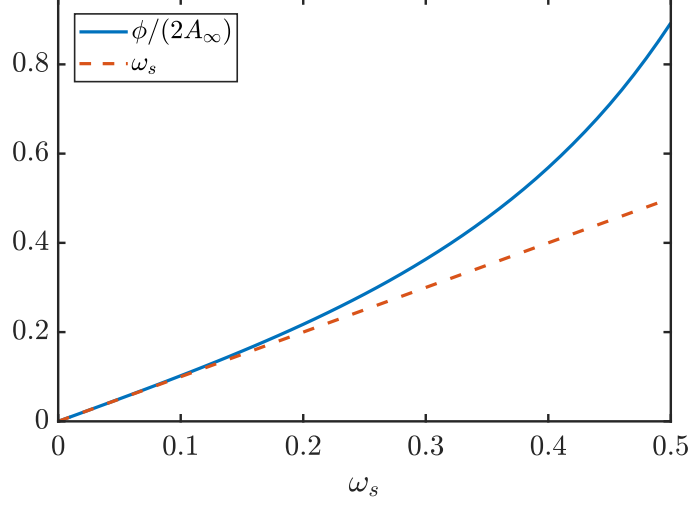


FIG. 5. Interference phase ϕ as a function of ω_s . A linear relation is found when $\omega_s < 0.1$.

In the next step we introduce the ladder operators

$$\hat{a} = \frac{1}{2} \left(x + iy + \frac{\partial}{\partial x} + i\frac{\partial}{\partial y} \right) \quad (11)$$

$$\hat{a}^\dagger = \frac{1}{2} \left(x - iy - \frac{\partial}{\partial x} + i\frac{\partial}{\partial y} \right) \quad (12)$$

$$\hat{b} = \frac{1}{2} \left(x - iy + \frac{\partial}{\partial x} - i\frac{\partial}{\partial y} \right) \quad (13)$$

$$\hat{b}^\dagger = \frac{1}{2} \left(x + iy - \frac{\partial}{\partial x} - i\frac{\partial}{\partial y} \right). \quad (14)$$

and the Hamiltonians (10), expressed in terms of these operators, acquire the following form:

$$\hat{h}'_{1,2} = (1 + \omega_s) \hat{a}^\dagger \hat{a} + (1 - \omega_s) \hat{b}^\dagger \hat{b} + 1 + \frac{R_p^2}{2} - \frac{R_p}{2} \left(\hat{a}^\dagger e^{\pm i\theta_p(t)} + \hat{a} e^{\mp i\theta_p(t)} + \hat{b}^\dagger e^{\mp i\theta_p(t)} + \hat{b} e^{\pm i\theta_p(t)} \right). \quad (15)$$

Both, h'_1 and h'_2 describe two sets of uncoupled, linearly driven oscillators. Their time evolution is solved via the ansatz $|\psi_j\rangle = e^{i\phi_j} |\alpha_j, \beta_j\rangle$. Here, ϕ_j is a global phase and $|\alpha_j\rangle$ and $|\beta_j\rangle$ are coherent states, i.e. eigenstates of the operators \hat{a} and \hat{b} , respectively. The dynamical evolution of the coherent state amplitudes and the phase is governed by the following equations:

$$\frac{d}{dt} \alpha_{1,2} = -i(1 + \omega_s) \alpha_{1,2} + i \frac{R_p}{2} e^{\pm i\theta_p}, \quad (16a)$$

$$\frac{d}{dt} \beta_{1,2} = -i(1 - \omega_s) \beta_{1,2} + i \frac{R_p}{2} e^{\mp i\theta_p}, \quad (16b)$$

$$\frac{d}{dt} \phi_{1,2} = \frac{R_p}{2} \text{Re} [\alpha_{1,2} e^{\mp i\theta_p} + \beta_{1,2} e^{\pm i\theta_p}]. \quad (16c)$$

By directly integrating these equations, we find the solutions,

$$\alpha_{1,2}(t) = \frac{R_p}{2(1+\omega_s)} \left[1 - i \int_0^t \dot{\theta}_p(t') e^{i(1+\omega_s)(t'-t) \pm i\theta_p(t')} dt' \right], \quad (17a)$$

$$\beta_{1,2}(t) = \frac{R_p}{2(1-\omega_s)} \left[1 + i \int_0^t \dot{\theta}_p(t') e^{i(1-\omega_s)(t'-t) \mp i\theta_p(t')} dt' \right], \quad (17b)$$

$$\phi_{1,2}(t) = \frac{R_p}{2} \operatorname{Re} \left[\int_0^t \alpha_{1,2}(t') e^{\mp i\theta_p(t')} + \beta_{1,2}(t') e^{\pm i\theta_p(t')} dt' \right]. \quad (17c)$$

Here, we have assumed that the oscillators are initially in their ground states and that $\theta_p(0) = 0$.

For a given driving profile $\theta_p(t)$ the above expressions can be evaluated either analytically (in special cases) or numerically. The result then allows us to calculate quantities such as the time-dependent spatial overlap between the two internal states,

$$\begin{aligned} \int \psi_1(\mathbf{r}) \psi_2^*(\mathbf{r}) d\mathbf{r} &= e^{i(\phi_1 - \phi_2)} \langle \alpha_2 | \alpha_1 \rangle \langle \beta_2 | \beta_1 \rangle \\ &= e^{i[\phi_1 - \phi_2 + \operatorname{Im}(\alpha_2^* \alpha_1 + \beta_2^* \beta_1)]} e^{-\frac{1}{2}(|\alpha_1 - \alpha_2|^2 + |\beta_1 - \beta_2|^2)}. \end{aligned} \quad (18)$$

The solution furthermore allows us to calculate the dependence of the interference phase ϕ on the rotation angular velocity ω_s , as is shown in Fig. 5. The discussion in the main text focusses on the linear regime which is achieved when $\omega_s < 0.1$.

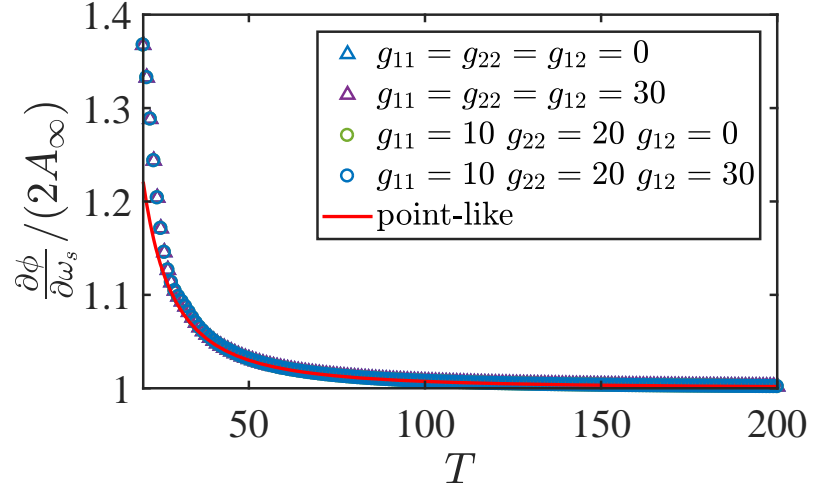


FIG. 6. Phase gradient as a function of the interrogation time T . The estimate based on a point-like particle subject to the centripetal force agrees well with numerical calculations and is largely independent from the presence or absence of interactions.

CLASSICAL ESTIMATE FOR THE INTERFERENCE PHASE

A "classical" estimate for the interference phase can be obtained by considering the motion of a point-particle (initially located at the trap center) along the ring. When rotating along the ring, the particle experiences a centripetal force (due to a finite angular momentum $R_p \dot{\theta}_p$) which will dynamically alter the radius R_p , i.e. the particle's displacement from the ring center. Balancing the centripetal and trapping forces (in the scaled units),

$$\dot{\theta}_p^2 R = (R - R_p). \quad (19)$$

we obtain the new radius to be $R = R_p / (1 - \dot{\theta}_p^2)$. As the radius is enlarged by a factor of $1/(1 - \dot{\theta}_p^2)$, the resulting enclosed area becomes,

$$A' = R_p^2 \int_0^T \frac{\dot{\theta}_p}{(1 - \dot{\theta}_p^2)^2} dt. \quad (20)$$

When $\dot{\theta}_p = \pi/T$, the area $A' = \pi R_p^2/[1 + (\pi/T)^2]^2$ is identical to the one used in Eq. (4) of the main text. Note, that this result is largely independent of atomic interactions, as shown in Fig. 6 and also Fig. 4b,d,f.

[1] A. D. Cronin, J. Schmiedmayer, and D. E. Pritchard, Rev. Mod. Phys. **81**, 1051 (2009).

[2] C. L. Degen, F. Reinhard, and P. Cappellaro, Rev. Mod. Phys. **89**, 035002 (2017).

[3] R. H. Parker, C. Yu, W. Zhong, B. Estey, and H. Müller, Science **360**, 191 (2018).

[4] Y. Bidel, N. Zahzam, C. Blanchard, A. Bonnin, M. Cadoret, A. Bresson, D. Rouxel, and M. F. Lequentrec-Lalancette, Nat. Commun. **9**, 627 (2018).

[5] B. Canuel, F. Leduc, D. Holleville, A. Gauguet, J. Fils, A. Virdis, A. Clairon, N. Dimarcq, C. J. Bordé, A. Landragin, and P. Bouyer, Phys. Rev. Lett. **97**, 010402 (2006).

[6] B. Fang, I. Dutta, P. Gillot, D. Savoie, J. Lautier, B. Cheng, C. L. Garrido Alzar, R. Geiger, S. Merlet, F. Pereira Dos Santos, and A. Landragin, J. Phys.: Conf. Ser. **723**, 012049 (2016).

[7] J. F. Clauser, Physica B **151**, 262 (1988).

[8] D. S. Durfee, Y. K. Shaham, and M. A. Kasevich, Phys. Rev. Lett. **97**, 240801 (2006).

[9] T. L. Gustavson, A. Landragin, and M. A. Kasevich, Class. Quantum Grav. **17**, 2385 (2000).

[10] I. Dutta, D. Savoie, B. Fang, B. Venon, C. L. Garrido Alzar, R. Geiger, and A. Landragin, Phys. Rev. Lett. **116**, 183003 (2016).

[11] D. Savoie, M. Altiorio, B. Fang, L. A. Sidorenkov, R. Geiger, and A. Landragin, arXiv:1808.10801 (2018).

[12] B. Barrett, R. Geiger, I. Dutta, M. Meunier, B. Canuel, A. Gauguet, P. Bouyer, and A. Landragin, Comptes Rendus Physique **15**, 875 (2014).

[13] T. Fernholz, R. Gerritsma, P. Krüger, and R. J. C. Spreeuw, Phys. Rev. A **75**, 063406 (2007).

[14] Y. Japha, O. Arzouan, Y. Avishai, and R. Folman, Phys. Rev. Lett **99**, 060402 (2007).

[15] O. Morizot, Y. Colombe, V. Lorent, H. Perrin, and B. M. Garraway, Phys. Rev. A **74**, 023617 (2006).

[16] A. S. Arnold, C. S. Garvie, and E. Riis, Phys. Rev. A **81**, 043608 (2006).

[17] J. H. T. Burke and C. A. Sackett, Phys. Rev. A **80**, 061603 (2009).

[18] B. E. Sherlock, M. Gildemeister, E. Owen, E. Nugent, and C. J. Foot, Physical Review A **83**, 043408 (2011).

[19] S. Eckel, J. G. Lee, F. Jendrzejewski, N. Murray, C. W. Clark, C. J. Lobb, W. D. Phillips, M. Edwards, and G. K. Campbell, Nature **506**, 200 (2014).

[20] R. Stevenson, M. R. Hush, T. Bishop, I. Lesanovsky, and T. Fernholz, Phys. Rev. Lett. **115**, 163001 (2015).

[21] C. Ryu and M. G. Boshier, New J. Phys. **17**, 092002 (2015).

[22] J. L. Helm, S. L. Cornish, and S. A. Gardiner, Phys. Rev. Lett. **114**, 134101 (2015).

[23] T. A. Bell, J. A. P. Glidden, L. Humbert, M. W. J. Bromley, S. A. Haine, M. J. Davis, T. W. Neely, M. A. Baker, and H. Rubinsztein-Dunlop, New J. Phys. **18**, 035003 (2016).

[24] P. Navez, S. Pandey, H. Mas, K. Poulios, T. Fernholz, and W. v. Klitzing, New Journal of Physics **18**, 075014 (2016).

[25] W. C. Campbell and P. Hamilton, J. Phys. B: At. Mol. Opt. Phys. **50**, 064002 (2017).

[26] H. Müller, S. W. Chiow, Q. Long, S. Herrmann, and S. Chu, Phys. Rev. Lett. **100**, 180405 (2008).

[27] S. Chiow, T. Kovachy, H. C. Chien, and M. A. Kasevich, Phys. Rev. Lett. **107**, 130403 (2008).

[28] M. Jaffe, V. Xu, P. Haslinger, H. Müller, and P. Hamilton, Phys. Rev. Lett. **121**, 040402 (2008).

[29] E. Bentine, T. L. Harte, K. Luksch, A. J. Barker, J. Mur-Petit, B. Yuen, and C. J. Foot, J. Phys. B: At. Mol. Opt. Phys. **50**, 094002 (2017).

[30] J. Williams, R. Walser, J. Cooper, E. A. Cornell, and M. Holland, Phys. Rev. A **61**, 033612 (2000).

[31] L. Salasnich, A. Parola, and L. Reatto, Phys. Rev. A **65**, 6 (2002).

[32] C. J. Pethick and H. Smith, *BoseEinstein Condensation in Dilute Gases* (Cambridge, 2008).

[33] Y. Che, F. Yao, H. Liang, G. Li, and X. Wang, Phys. Rev. A **98**, 053609 (2018).

[34] D. W. Boeringer and D. H. Werner, in *IEEE Antennas Propag. Soc. Symp. 2004.*, Vol. 3 (IEEE, 2004) pp. 2293–2296.

[35] N. Wiebe and C. Granade, Phys. Rev. Lett. **117**, 010503 (2016).

[36] A. Lumino, E. Polino, A. S. Rab, G. Milani, N. Spagnolo, N. Wiebe, and F. Sciarrino, Phys. Rev. Appl. **10**, 044033 (2018).

[37] D. Döring, G. McDonald, J. E. Debs, C. Figl, P. A. Altin, H.-A. Bachor, N. P. Robins, and J. D. Close, Phys. Rev. A **81**, 043633 (2010).

[38] E. Rocco, R. N. Palmer, T. Valenzuela, V. Boyer, A. Freise, and K. Bongs, New Journal of Physics **16**, 093046 (2014).